

# Linear and nonlinear second-order polarizabilities of hemispherical and sector-shaped metal nanoparticles

J. Jayabalan, Manoranjan P. Singh, and Arup Banerjee

*Laser Physics Applications Division, Raja Ramanna Centre for Advanced Technology, Indore-452013, India*

K. C. Rustagi

*Department of Physics, Indian Institute of Technology-Bombay, Mumbai 400076, India*

(Received 19 July 2007; published 23 January 2008)

In this paper, we present results of calculations of linear and second-order nonlinear polarizabilities of sector-shaped metallic nanoparticles (hemisphere is a special case) using free electron theory. The dependences of the ground state electron density distribution and polarizabilities on various shape parameters of sector are analyzed. The ground state electron densities near the corners and edges of sector-shaped nanoparticle are very low and do not contribute to the linear and second-order polarizabilities. The second-order polarizability is found to depend strongly on the angle of the sector and is shown to be proportional to the product of an appropriately defined asymmetric volume of the particle and the third power of the electron cloud length.

DOI: [10.1103/PhysRevB.77.045421](https://doi.org/10.1103/PhysRevB.77.045421)

PACS number(s): 73.21.La, 73.22.Dj, 42.65.An

## I. INTRODUCTION

Optical properties of the metallic nanostructures can be controlled by changing their sizes, shapes, host media, and distributions.<sup>1-6</sup> The modifications of the linear and third-order nonlinear optical properties arising due to confinement of electrons in spherical nanoparticle are known for a long time.<sup>7-10</sup> The advancement in the nanoparticle preparation and characterization techniques has now made it possible to obtain particles of various other shapes.<sup>11-15</sup> This development has motivated several theoretical<sup>16,17</sup> and experimental<sup>4,5,18</sup> studies focusing on the effect of shapes and sizes of nanoparticles on the optical properties.

There are two types of confinements which strongly affect the optical properties of nanoparticles, namely, quantum confinement and dielectric confinement. The quantum confinement arises due to localized confining potential for electrons and results in discrete atomlike energy levels. This makes the linear and nonlinear dielectric properties of the nanoparticle significantly different from those of the bulk. On the other hand, dielectric confinement is caused by a difference in the values of dielectric constants of the particle and the host media. Because of this, a different local field is seen by the electrons as compared to the applied one. To understand the optical properties of nanostructures, it is necessary to take into account both the confinements.

The dielectric confinement gets modified by the shape, size, and dielectric constant of the host media, which results in the splitting or the shifting of the surface plasmon resonance (SPR) peaks. The shifting of SPR peak has been exploited for biosensing applications.<sup>19</sup> For example, Miller and Lazarides showed that the sensitivity of this shift depends on the dispersion of the real part of dielectric constant.<sup>20</sup> We note that for particles with sizes more than tens of nanometers, the real part of dielectric constant is same as that of bulk. On the other hand, for particles with sizes of a few nanometers, the dielectric constant depends strongly on its shape and size. This provides an additional control for improving the sensitivity in biosensing applica-

tions. It is necessary to have better understanding of the effect of shape on the dielectric constants of a nanoparticle.

Recently, there have been several studies devoted to the nonlinear optical properties of nanoparticles. Among these, studies aimed at finding out shapes possessing large second-order susceptibility at wavelengths near the particle's plasmon resonance are of particular interest.<sup>21,22</sup> Second harmonic generation efficiency of thin metallic wedge arrays has been studied by Zheludev and Emel'yanov.<sup>23</sup> They have shown that it depends strongly on the shape and size of the nanoparticle. Kuiru *et al.* have theoretically shown that three spheres of decreasing radii arranged in a row can act as an efficient nanolens and it can also have high hyperpolarizability at its local field resonance.<sup>22</sup>

The main aim of this paper is to understand the dependence of linear and nonlinear optical properties on the shape of sector-shaped nanoparticle. A sector shape is a part of a spherical particle enclosed by two constant azimuthal angle planes at  $\phi = \phi_0/2$  and  $\phi = -\phi_0/2$  as shown in Fig. 1. Note that hemispherical nanoparticle is a special case of a sector-shaped particle, with  $\phi_0 = \pi$ . Hemispherical dots are of special interest since these can be grown and deposited on suitable substrates by several methods. We analyze the dependence of the ground state electron density distribution and polarizabilities on various shape parameters of sector. The scaling behavior of linear polarizability with respect to the size of the sector-shaped particle has been studied. To characterize the asymmetry in a particle quantitatively, we introduce a quantity called asymmetric volume which is analog to the *asymmetric area* proposed in our previous paper related to the wedge-shaped particle.<sup>17</sup> Using asymmetric volume, we find a scaling behavior of second-order polarizability with respect to the shape and size of the particle. The rest of the paper is organized in the following manner. The wave functions and the method by which the polarizabilities are calculated are presented in Sec. II. In Sec. III, we present and discuss the results of calculation. The paper is concluded in Sec. IV. A brief derivation of second-order polarizability using the single-particle wave functions is given in the Appendix.

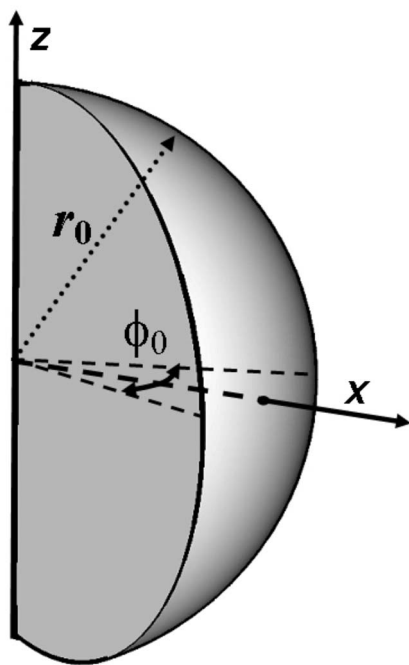


FIG. 1. The sector-shaped nanoparticle, with radius the  $r_0$ . The corner along the  $z$  axis has azimuthal angle  $\phi_0 = \pi/X$ .

## II. GENERAL FORMULATION

### A. Wave functions and energies

We consider a system of  $N$  noninteracting electrons confined inside a hard walled sector-shaped region of radius  $r_0$  and azimuthal angle  $\phi_0$  as shown in Fig. 1. The single-particle wave functions for this system can be determined from the Schrödinger equation:

$$H\Psi_i = E_i\Psi_i, \quad (1)$$

with the Hamiltonian

$$H = -\frac{\hbar^2}{2m_o}\nabla^2 + V(\mathbf{r}), \quad (2)$$

where  $\Psi_i$  is the  $i$ th single-particle wave function and  $m_o$  is the effective mass of the electron. The confining potential is given by  $V(\mathbf{r})=0$  for  $|\phi| < \phi_0/2$  and  $r < r_0$  and  $V(\mathbf{r})=\infty$  otherwise. In accordance with this potential, the wave functions should satisfy the following boundary conditions:

$$\Psi(\theta, \phi, r_0) = 0 \quad \text{and} \quad \Psi\left(\theta, \pm \frac{\phi_0}{2}, r\right) = 0. \quad (3)$$

The normalized single-particle wave functions obtained by solving Eq. (1) are

$$\Psi_{m_l s} = \frac{\sqrt{2X(2l+1)(l-m)!}}{j_{l+1}(k_{s_l}r_0)\sqrt{\pi r_0^3(l+m)!}} \zeta_m(\phi) P_l^m(\cos \theta) j_l(k_{s_l}r), \quad (4)$$

with

$$k_{s_l} = \alpha_{s_l}/r_0, \quad \phi_0 = \pi/X, \quad X = 1, 2, 3, \dots,$$

$$m = nX, \quad l = m, m+1, m+2, \dots,$$

$$s = 1, 2, \dots, \quad \text{and} \quad n = 1, 2, \dots,$$

where  $j_l$  is the spherical Bessel function of order  $l$ ,  $P_l^m$  is the associated Legendre function of order  $l$  and degree  $m$ , and  $\alpha_{s_l}$  is the  $s$ th zero of  $l$ th order spherical Bessel function. For computational simplicity, we have taken  $\phi_0$  to be  $\pi/X$  with  $X$  taking integral values.

The azimuthal part of the wave function is given by

$$\zeta_{nX}(\phi) = \begin{cases} (-1)^{(n+1)/2} \cos(nX\phi) & \text{when } n \text{ is odd} \\ (-1)^{n/2} \sin(nX\phi) & \text{when } n \text{ is even.} \end{cases} \quad (5)$$

The corresponding eigenenergies are given by

$$E_{ls} = \frac{\hbar^2 \alpha_{s_l}^2}{2m_o r_0^2}. \quad (6)$$

The degeneracy of each energy level is given by the integer part of  $(l/X)$ . We note that the forms of the wave functions for electrons confined in a sector-shaped particle are similar to those for a spherical nanoparticle.<sup>9</sup> In fact, the wave functions for the sector-shaped particle are subset of the wave functions for spherical nanoparticle which satisfy the additional boundary conditions specified by Eq. (3). The additional constraint on  $|\phi|$  forces the azimuthal part of wave functions of electrons in sectors to be of definite parity  $\sin(m\phi)$  or  $\cos(m\phi)$  instead of  $\exp(-im\phi)$ .

### B. Dipole matrix elements and selection rules

The linear and second-order polarizabilities are calculated by employing the analytical expressions given by

$$\alpha_{\sigma\sigma} = \frac{1}{\epsilon_0 \hbar} \sum_{ia} \left\{ \frac{M_{ia}^\sigma M_{ai}^\sigma}{\omega_{ai} + \omega} + \frac{M_{ia}^\sigma M_{ai}^\sigma}{\omega_{ai} - \omega} \right\}, \quad (7)$$

and

$$\beta_{\sigma\sigma\sigma}(-2\omega; \omega, \omega) = \frac{-1}{2\hbar^2 \epsilon_0} \left\{ \sum_{iab} \left[ \frac{M_{ab}^\sigma M_{ia}^\sigma M_{bi}^\sigma}{(\omega_{ia} + 2\omega)(\omega_{bi} - \omega)} \right. \right. \\ + \frac{M_{ab}^\sigma M_{ia}^\sigma M_{bi}^\sigma}{(\omega_{ia} - \omega)(\omega_{bi} + 2\omega)} \\ + \left. \frac{M_{ab}^\sigma M_{ia}^\sigma M_{bi}^\sigma}{(\omega_{ia} - \omega)(\omega_{bi} - \omega)} \right] \\ - \sum_{ija} \left[ \frac{M_{ij}^\sigma M_{ia}^\sigma M_{aj}^\sigma}{(\omega_{ia} + 2\omega)(\omega_{aj} - \omega)} \right. \\ + \frac{M_{ij}^\sigma M_{ia}^\sigma M_{aj}^\sigma}{(\omega_{ja} - \omega)(\omega_{ai} + 2\omega)} \\ + \frac{M_{ij}^\sigma M_{ia}^\sigma M_{aj}^\sigma}{2(\omega_{ja} - \omega)(\omega_{ai} - \omega)} \\ + \left. \left. \frac{M_{ij}^\sigma M_{ia}^\sigma M_{aj}^\sigma}{2(\omega_{ia} - \omega)(\omega_{aj} - \omega)} \right] \right\}, \quad (8)$$

respectively, where  $\sigma$  represent the Cartesian component,  $x$ ,

$y$ , or  $z$ ,  $i$  and  $j$  represent all the occupied single-particle states, while  $a$  and  $b$  represent all the unoccupied single-particle states of the system. The frequency  $\omega_{\mu\nu} [(E_\mu - E_\nu)/\hbar]$  is the energy separation between the levels  $\mu$  and  $\nu$ , and the frequency of the applied field is denoted by  $\omega$ . The dipole matrix element between levels  $\mu$  and  $\nu$  along the direction of  $\sigma$  is denoted by  $M_{\mu\nu}^\sigma$ , and  $\epsilon_0$  is the permittivity of free space. Note that in the above expression, all the transitions are between the occupied and unoccupied levels, thereby avoiding any numerical instability at spurious resonances. These expressions have been obtained by applying time-dependent perturbation theory to the canonical form of single-particle Schrödinger equation.<sup>24,25</sup> In deriving these expressions, gauge invariance of the orbitals has been exploited.<sup>25</sup> A brief derivation of these expressions is presented in the Appendix.

For calculating linear and second-order polarizabilities, we need to calculate different directional components of dipole matrix elements. In spherical coordinates, the dipole matrix elements can be written as

$$M_{(lns)(l'n's')}^\sigma = e\Phi_{n,n'}^\sigma \Theta_{ln;l'n'}^\sigma R_{ls;l's'}^\sigma, \quad (9)$$

where  $\Phi_{n,n'}^\sigma$ ,  $\Theta_{ls;l's'}^\sigma$  and  $R_{ls;l's'}^\sigma$  are the azimuthal, polar angle, and radial parts of the dipole matrix element, respectively. The azimuthal parts of dipole matrix element along the  $x$  and  $y$  directions are the same as that of the wedge case.<sup>17</sup> Further, due to the parity,  $\Phi_{n,n'}^x$  is nonzero only when both  $n$  and  $n'$  are either odd or even integers ( $\Delta n = n - n'$  is even). Similarly,  $\Phi_{n,n'}^y$  is nonzero only when  $\Delta n$  is odd. On the other hand, for the  $z$  direction,

$$\begin{aligned} \Phi_{n,n'}^z &= \frac{2X}{\pi} \int_{-\pi/2X}^{\pi/2X} \zeta_n(\phi) \zeta_{n'}(\phi) d\phi, \\ &= \delta_{nn'}, \end{aligned} \quad (10)$$

where  $\delta_{nn'}$  is the Kronecker delta.

The radial part of the dipole matrix element is the same for all the three directions, and it is given by

$$R_{ls;l's'}^\mu = \frac{2}{r_0^3 j_{l+1}(k_{ls}r_0) j_{l'+1}(k_{l's'}r_0)} \int_0^{r_0} r^3 j_l(k_{ls}r) j_{l'}(k_{l's'}r) dr. \quad (11)$$

For transition between two different levels, the above integration can be carried out by using approximate expansions for Bessel functions as used by Hache.<sup>9</sup> Later, Barma and Subrahmanyam<sup>10</sup> showed that the Debye expansion for the large-order Bessel functions is more accurate than the approximation used by Hache. However, all of these expressions have limited use in our case because for calculating the second-order polarizability, we also need radial matrix element between the same level, so we evaluate these integrals numerically.

The polar angle parts of the dipole matrix element along the  $x$  and  $y$  directions are the same, and they are calculated numerically by using the following expression:

TABLE I. Selection rules for the quantum numbers  $l$  and  $n$  of sector-shaped particles.

	$x$ direction	$y$ direction	$z$ direction
$\Delta n$	Even	Odd	0
$\Delta l$	Even	Even if $X$ is even; odd if $X$ is odd	Odd

$$\begin{aligned} \Theta_{ln;l'n'} &= \frac{\sqrt{(2l+1)(2l'+1)(l-m)!(l'-m)!}}{2\sqrt{(l+m)!(l'+m)!}} \\ &\times \int_{-1}^1 P_l^{nX}(t) P_{l'}^{n'X}(t) \sqrt{1-t^2} dt. \end{aligned} \quad (12)$$

Using the parity of associated Legendre polynomial, we find that  $\Theta_{ln;l'n'}$  is nonzero only when  $(l+nX)$  and  $(l'+n'X)$  are both even or both odd integers. Finally, the angular part of the dipole matrix in the  $z$  direction,  $\Theta_{ln;l'n'}^z$ , is given by

$$\begin{aligned} \Theta_{ln;l'n}^z &= \frac{\sqrt{(2l+1)(2l'+1)(l-m)!(l'-m)!}}{2\sqrt{(l+m)!(l'+m)!}} \\ &\times \int_{\tau}^1 t P_l^{nX}(t) P_{l'}^{nX}(t) dt. \end{aligned} \quad (13)$$

This integration has been carried out by using recurrence relation of  $P_l^m$  and the condition  $\Delta n = 0$  resulting in

$$\Theta_{ln;l'n}^z = C_{l'}^m \delta_{l+1,l'} + C_l^m \delta_{l,l'+1}, \quad (14)$$

with

$$C_l^m = \sqrt{\frac{l^2 - m^2}{4l^2 - 1}}. \quad (15)$$

Thus, the nonzero matrix elements exist only for  $\Delta l = l - l' = 1$ . For the convenience of readers, all these selection rules are summarized in Table I.

### III. RESULTS AND DISCUSSIONS

Before discussing the results in detail, we mention that all the results presented in this paper are obtained by considering the electron density inside the sector to be same as that of bulk silver. The single-particle states are filled according to the Pauli's exclusion principle. The nanoparticle is assumed to be at 0 K so that all the levels below the Fermi level are filled and those above it are empty. For our purpose, we consider sector-shaped particles with various sizes with the uppermost level fully occupied.<sup>26</sup>

#### A. Ground state electron density distribution

The electron density distribution  $D(r, \theta, \phi)$  corresponding to the ground state of a nanoparticle at 0 K is given by

$$D(r, \theta, \phi) = \sum_i |\Psi_i(r, \theta, \phi)|^2, \quad (16)$$

where  $i$  runs over all the occupied states of the system. In Fig. 2, we show sections of electron density distribution in

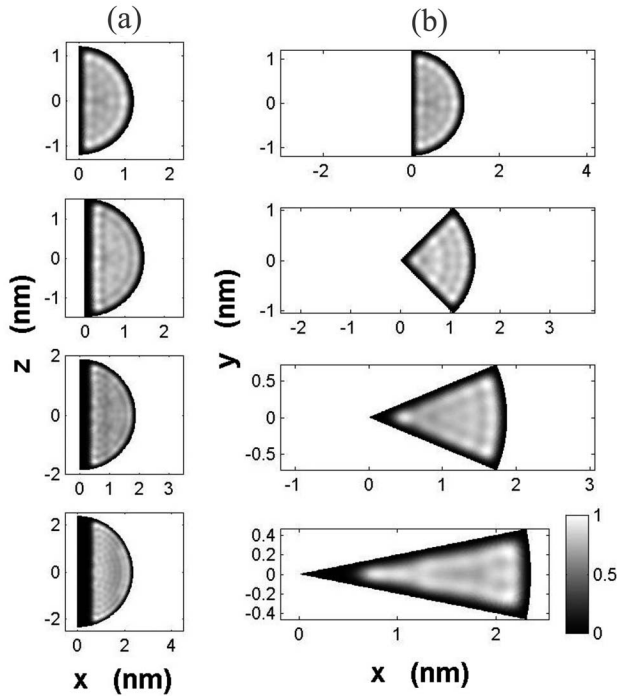


FIG. 2. The ground state electron density distribution of sector-shaped nanoparticle with nearly the same volume for different azimuthal angles:  $\phi_0 = \pi$ ,  $\phi_0 = \pi/2$ ,  $\phi_0 = \pi/4$ , and  $\phi_0 = \pi/8$  from top to bottom along the (a)  $y=0$  plane and (b)  $z=0$  plane. Note that the electron densities near the edges and corners are very small. These low electron density regions are more appreciable for particles with smaller apex angle.

two planes, namely,  $y=0$  and  $z=0$  for sectors with  $X=1, 2, 4$ , and  $8$  containing nearly 200 electrons. For  $X=1$  (hemisphere), both the planes are equivalent and it is expected that the density of electrons is the same. This is seen in Fig. 2. The figure also shows that for all the cases, the electron density is almost zero near the edges and at the corners. Moreover, the sizes of the low-density regions increase as the azimuthal angle  $\phi_0$  reduces. This can be explained by noting that the electron which has the smallest de Broglie wavelength is the one in the Fermi level. The diffraction limit of the electron wave forbids the electron to enter the corners and edges where the space is narrower than half of the Fermi wavelength of electron. When the azimuthal angle of the particle is reduced, the narrow region increases. The lowering of electron density near the sharp corner for larger  $X$  can also be explained in terms of the wave functions of the electrons. We note that for a sector-shaped particle, the minimum value of the quantum number  $l$  is  $X$ . The first peak of the function  $j_l k_{s,l} r$  occurs at larger values of  $k_{s,l} r$  for large  $l$ . Thus, for a sector with large  $X$ , hence large  $l$ , the density of electron cloud is pushed away from the apex  $r=0$ .

To quantify the length of the low-density region, we define an effective length  $x_r$  from the corner ( $r=0$ ) as shown in Fig. 3(a). From this figure, simple geometrical considerations yield

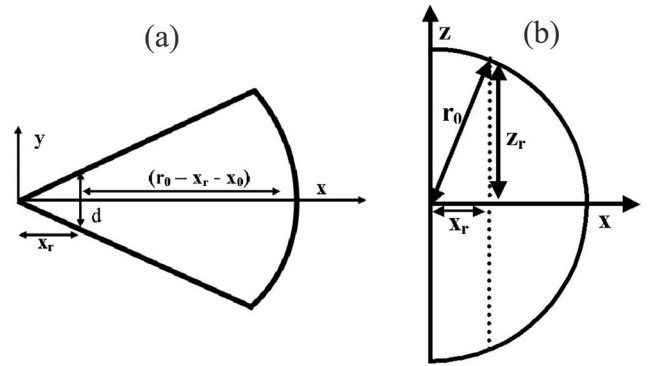


FIG. 3. The sections (a)  $z=0$  and (b)  $y=0$  of a sector-shaped nanoparticle with  $\phi_0 = \pi/X$ . For details about different lengths, read the text.

$$x_r(X) = \frac{d}{2 \tan\left(\frac{\pi}{2X}\right)}. \quad (17)$$

In the above expression,  $d$  is the space between the sides of the nanoparticle where the electron density is below a certain cutoff value. Evaluation of the parameter  $d$  will be discussed in more detail in the next section. The length  $x_r$  plays an important role in determining the scaling behavior of linear polarizabilities.

## B. Polarizabilities

In this section, we study the shape dependence of various components of the linear polarizability  $\alpha$  and second-order polarizability  $\beta$  of sector-shaped particles by making use of Eqs. (7) and (8), respectively. The summations in Eqs. (7) and (8) are performed over finite number of levels above and below the Fermi level. The convergence is checked by including more number of levels in the summation.

From the selection rules on  $\Delta l$  and  $\Delta n$  (see Table I), it is easy to note that if transition is allowed between a pair of levels for applied field in any of the Cartesian directions, then it is forbidden for the fields applied along the other two directions. For a field in the  $xz$  plane, the transition matrix elements are nonvanishing only if  $\Delta n$  is even (including zero), but for a field applied along the  $y$  direction,  $\Delta n$  should be odd. Hence, a pair of levels for which if a transition is allowed for a field along the  $y$  direction, then, the transitions corresponding to the field along the other two directions are forbidden. Moreover, due to the selection rule on  $\Delta l$  if a transition is allowed between a pair of levels for field along the  $x$  direction, then, it is forbidden for the field applied along the  $z$  direction. As a result of this, the chosen coordinate system renders a diagonal representation for the linear polarizability tensor. A sector-shaped particle has inversion symmetry along the  $y$  and  $z$  directions; the nonzero components of second-order polarizabilities are  $\beta_{xxx}$ ,  $\beta_{yyy}$ , and  $\beta_{zzz}$  and their permutations. This is also consistent with the selection rules described above.

The linear polarizability for a cube-shaped particle has been calculated by Genzel *et al.*<sup>7</sup> They have shown that the

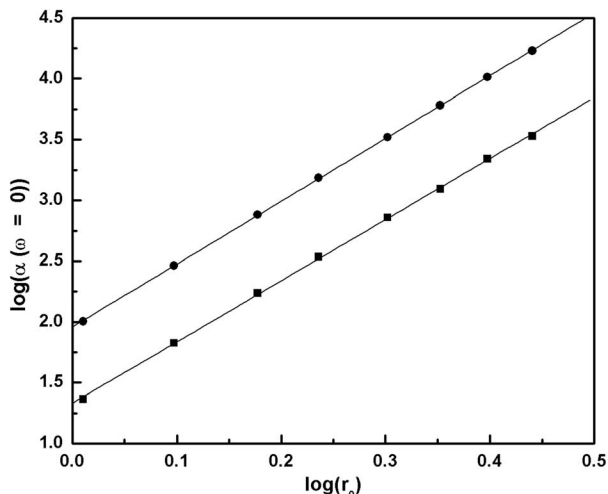


FIG. 4. Plot of the logarithm of the linear polarizability as a function of the logarithm of the radius of the particle. The squares and solid circles represent  $\alpha_{xx}$  and  $\alpha_{yy}$ , respectively. The lines denote the least squares fits of the calculated data.

static value of linear polarizability is directly proportional to the square of the length of the cube and the number of electrons inside the cube. Similar scaling has been observed for particles with other shapes.<sup>8</sup> For hemisphere of radius  $r_0$ , the lengths of the particle along the  $x$  and  $y$  directions are  $r_0$  and  $2r_0$ , respectively, and the number of electrons inside the hemisphere is proportional to  $r_0^3$ . Thus, the static polarizabilities  $\alpha_{xx}$  and  $\alpha_{yy}$  ( $=\alpha_{zz}$ ) should vary as  $r_0^5$ . To illustrate this, in Fig. 4, we plot the logarithm of static polarizabilities  $\alpha_{xx}$  and  $\alpha_{yy}$  as a function of logarithm of  $r_0$  along with the corresponding least squares fitted lines. The slopes of the fitted lines for  $\alpha_{xx}$  and  $\alpha_{yy}$  are found to be 5.03 and 5.16, respectively, implying that the linear polarizability is nearly proportional to  $r_0^5$ .

Next, we consider sector-shaped particles with different values of  $X$  containing nearly 200 electrons. As stated earlier, the radius of the particle is slightly adjusted till the last level is completely filled. Due to this, the volume of the particles varies by about 2%. In Fig. 5, we show the variation of static polarizability  $\alpha_{xx}$  with  $X$ . From the above discussion on the scaling behavior of static polarizabilities, it is expected that for a given volume,  $\alpha_{xx}$  should scale as  $r_0^2$ . Using the fact that  $r_0$  is proportional to  $\sqrt[3]{X}$ , we fit our calculated data in Fig. 5 with  $ar_0^2$ , with  $a$  being the fitting parameter. Figure 5 clearly shows that the fitting is not very good especially for large values of  $X$ . The reason behind this mismatch may be due to the fact that the effective length of the electron distribution is shorter than the actual length of the particle. Note that the difference between the two lengths is more for the particle with larger  $X$ , which is consistent with the result presented in Fig. 5. In order to deduce a scaling law, we define an effective length  $r_{eff}$  of the particle along the  $x$  direction as  $[r_0 - x_r(X) - x_0]$ , where the parameter  $x_0$  characterizes the length of low electron density region which is independent of  $X$ . A fit to  $\alpha_{xx}$  with the function  $a r_{eff}^2$ , with  $a$ ,  $d$ , and  $x_0$  as fitting parameters, is shown in Fig. 5. The best fitted points are

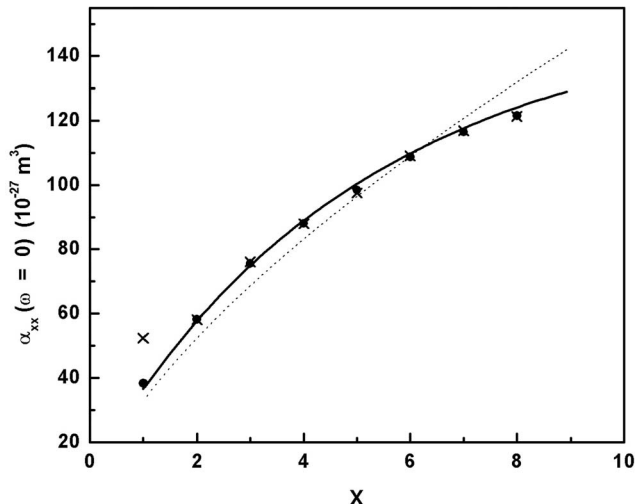


FIG. 5. The plot of static value of  $\alpha_{xx}$  for sector-shaped nanoparticles with the same volume as a function of  $X$ . The crosses are the theoretically calculated values of  $\alpha_{xx}$ . The dotted and solid lines are fit to  $\alpha_{xx}$  with  $ar_0^2$  and  $a(r_0^2 - r_{eff}^2)$ , respectively. The solid circles are the fitted points with the exact radius of the particle taken into account.

obtained by taking into account the volume corrections, and the results are also displayed by crosses in Fig. 5. The best fit value for the parameter  $d$  is found to be 0.2 nm. Next, we focus our attention on the scaling behavior of  $\alpha_{zz}$ . To this end, we plot  $\alpha_{zz}$  as a function of  $X$  in Fig. 6. Similar to the effective length of electron cloud in the  $x$  direction, we geometrically express the effective length of electron cloud in the  $z$  direction ( $z_r$ ) as  $\sqrt{(r_0^2 - x_r^2)}$  [see Fig. 3(b)]. The results of our calculations are fitted with the function  $az_r^2$ , and the results are displayed in Fig. 6. For this case, the best fit value of  $d$  is found to be 0.32 nm. Note that the values of the parameter  $d$  obtained in both the cases are of the order of half of the Fermi wavelength of the electron in bulk, which is

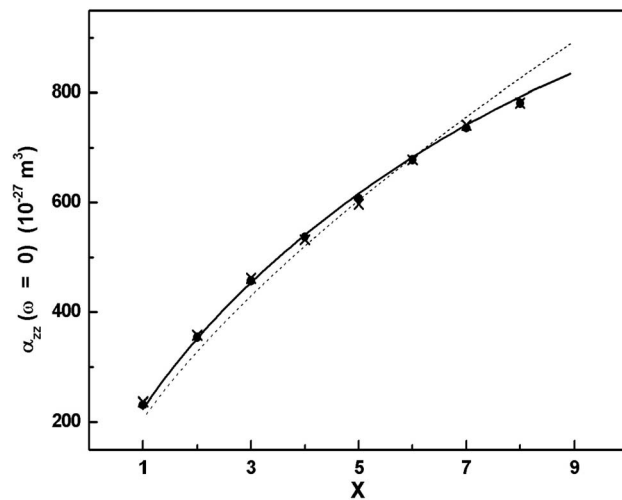


FIG. 6. Same as Fig. 5 but for  $\alpha_{zz}$ . The dotted and solid lines are fit to  $\alpha_{zz}$  with  $ar_0^2$  and  $a(r_0^2 - r_{eff}^2)$ , respectively.

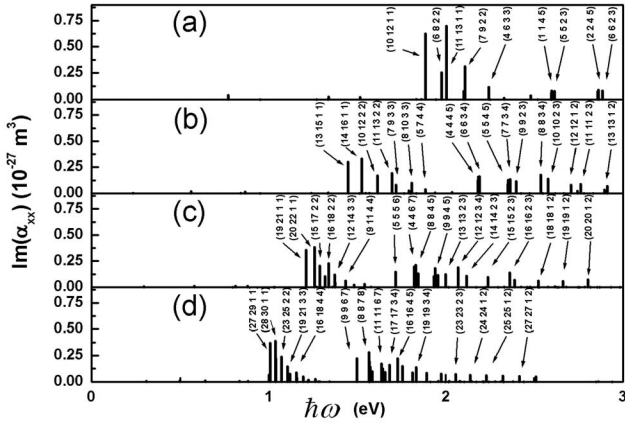


FIG. 7. The resonance peak positions of  $\alpha_{xx}$  for sector-shaped nanoparticles with same volume but different values of  $X$  and  $r_0$ : (a)  $X=1$ ,  $r_0=1.2034$  nm; (b)  $X=2$ ,  $r_0=1.4971$  nm; (c)  $X=4$ ,  $r_0=1.8739$  nm; (d)  $X=8$ ,  $r_0=2.3532$  nm. The height of the vertical lines represents the strength of transitions. The numbers on the top of these vertical lines are the quantum numbers  $l$  and  $s$  of the levels  $i$  and  $j$  involved in these transitions given in the order  $(l_i, l_j, s_i, s_j)$ .

0.26 nm.<sup>27</sup> At this point, we would like to mention that in Refs. 28 and 29, the calculations of plasmon resonances of two dimensional odd-shaped particles are performed with the corners rounded by 0.25 nm to avoid numerical difficulties. Our observation of smoothing of corners for electron cloud provides justification for their rounding of the corners. Further, we note that only for the case of sector with  $X=1$  there is a deviation from the smooth behavior and can be attributed to the disappearance of the corner.

Further, to test the applicability of the fitting function proposed above to other shapes, we carry out fitting the results of static polarizability of wedge-shaped particle.<sup>17</sup> We find that for wedge-shaped particles also, the fitting function incorporating the length correction is better suited. In reality, the confining potential does not have any sharp corners or edges due to the finite size of atom. We are approximating a real cluster by a geometric shape, so sharp edge is a consequence of our modeling. The ground state electron density distribution, as well as the behavior of linear polarizability, shows that approximating the tip of the nanostructure by sharp edges does not matter since regions smaller than atomic size is not occupied anyway.

Next, we focus our attention on the frequency dependence of the polarizability. In Fig. 7, we show the frequencies and the corresponding strengths of polarizability  $\alpha_{xx}$  for sector-shaped particles with  $X=1, 2, 4$ , and  $8$ . The values of the radii of the particles are 1.2034, 1.4971, 1.8739, and 2.3532 nm, respectively. The height of the vertical lines in Fig. 7 represents the strength of the transition given by  $|M_{\mu\nu}^\lambda|^2$ , and each vertical line is characterized by the quantum numbers  $l$  and  $s$  of levels  $\mu$  and  $\nu$  in the order  $[l(\mu), l(\nu), s(\mu), s(\nu)]$ . Each transition is obtained by summing  $|M_{\mu\nu}^\lambda|^2$  over all possible values of the quantum number  $n$ . We note from Fig. 7 that the position of the first strong transition gets redshifted as the value of  $X$  increases. This is similar to the case of a particle in a box, where energy of a

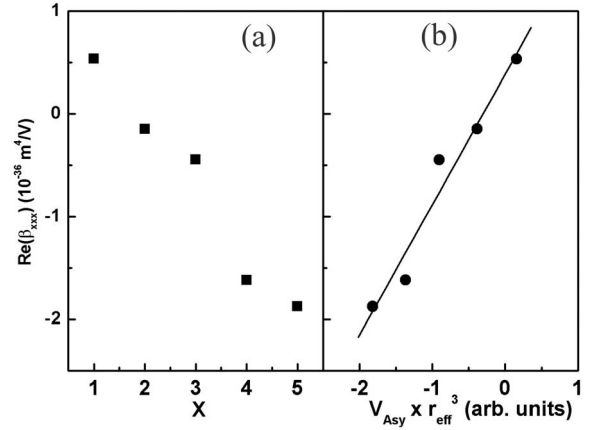


FIG. 8. Variation of real part of  $\beta_{xxx}$  at zero frequency for sector-shaped particle with nearly the same volume as a function of  $X$ . (b) The plot between the above mentioned  $\beta_{xxx}$  and  $V_{Asy} r_{eff}^3$ . The solid line is the least squares fit for the calculated data.

given level is inversely proportional to the square of length of the particle [see Eq. (6)]. As a result of this, the difference between the energies also increases as the radius of the particle is reduced. The strengths of transitions for  $\Delta n \neq 0$  are much weaker as compared to the transition corresponding  $\Delta n=0$ . For sectors with large  $X$ , the oscillator strength of the transitions satisfying  $\Delta n=0$  becomes even more stronger than the other cases. This observation can be explained by looking at the expression for the azimuthal part of dipole matrix elements, which, for  $\Delta n=0$ , is given by

$$\Phi_{n,n'}^x \approx 1 + \frac{1}{4n^2 X^2 - 1}. \quad (18)$$

On the other hand, for  $\Delta n \neq 0$  and  $X \gg 1$ , it is given by

$$\Phi_{n,n'}^x \approx \frac{-1}{X^2 \Delta n^2}. \quad (19)$$

A comparison of these two expressions clearly shows that for large  $X$ ,  $\Phi_{n,n'}^x$  for  $\Delta n=0$  has a term independent of  $X$  and  $n$  resulting in higher value of the matrix element. Notice further from Fig. 7 that the transitions can be grouped into two bunches. The lower energy bunch is comprised of transitions, with  $s_i=s_j$  and  $|l_i-l_j|=2$ , whereas the transitions with  $l_i=l_j$  and  $|s_i-s_j|=1$  form the high energy bunch.

Having discussed the static and frequency dependent linear polarizability of sector-shaped particles, we now present the results of our calculation for the second-order nonlinear polarizability. In Fig. 8(a), we show the variation of real part of  $\beta_{xxx}$  at zero frequency for sectors with different values of  $X$ . The sign of  $\beta_{xxx}$  is positive for the hemisphere case ( $X=1$ ), whereas for all other sectors it is negative. The magnitude of  $\beta_{xxx}$  increases smoothly as  $X$  increases, except for the hemisphere case, for which the magnitude is higher than that for  $X=2$  case. This can be explained by an argument similar to that of asymmetric area (in this case, asymmetric volume) presented earlier.<sup>17</sup> In Ref. 17, we discussed a possible way of characterizing the asymmetry of a particle which qualitatively explains the behavior of second-order polarizability.

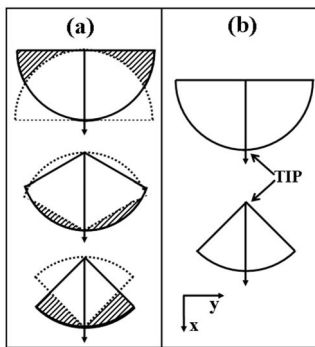


FIG. 9. A geometric explanation for how the shape of the sector decides the magnitude and sign of  $\beta_{xxx}$ . For clarity, we show the section of sector in the  $z=0$  plane. (a) Sector-shaped nanoparticles and their corresponding reflected images through a plane at  $x=r_0/2$  as solid and dashed lines for three azimuthal angles:  $\phi_0=\pi$ ,  $\phi_0=2\pi/3$ , and  $\phi_0=\pi/2$ . The shaded region represents the nonoverlapping volume which is the asymmetric volume of the particle. (b) The position of the tip on hemisphere and  $\phi_0=\pi/2$  case.

For this purpose, we first calculate the asymmetric volume  $V_{asy}$  of a sector-shaped particle. In order to do this, we consider reflection of the particle by a plane perpendicular to the  $x$  axis at  $r_0/2$ . Then, the reflected image is superposed on the original particle. This prescription is illustrated in Fig. 9(a) for sector with different azimuthal angles, where we show cross section of the particle at the  $z=0$  plane. The nonoverlapping volume of these two superimposed images constitutes the  $V_{asy}$  of a given sector. Asymmetric volume calculated in this way is more for the hemisphere case ( $X=1$ ) than that for the sector having  $X=2$ . This is consistent with the result that  $\beta_{xxx}$  is larger for hemisphere than the particle with  $X=2$ . In order to explain the difference in sign of  $\beta_{xxx}$  for hemisphere compared to other sector-shaped particles, we show the cross section of the particle at  $z=0$  plane of a hemisphere and sector with  $X=2$  in Fig. 9(b). In contrast to the other sector-shaped particles, note that for hemisphere, there exists no tip at  $x=0$ . Hence, for hemisphere, an effective tip can be identified at  $x=r_0$  as shown in Fig. 9(b). It is this difference in the location of tip in a hemisphere and other sectors which gives rise to different signs for  $\beta_{xxx}$ . In other words, when one moves from origin toward the positive  $x$  direction, the space available for the electron decreases in hemisphere, while for the other sectors, it increases. This reversal in the direction leads to change of sign of  $\beta_{xxx}$ . Furthermore, second-order polarizability involves product of three dipole matrix elements [Eq. (8)], and it is therefore expected that  $\beta$  should also depend on the third power of electron cloud length. With these scaling behaviors, we expect that  $\beta_{xxx}$  should be proportional to the product of asymmetric volume and the third power of electron cloud length. Figure 8(b) shows dependence of  $\beta_{xxx}$  on  $V_{asy} \times r_{eff}^3$  for sector-shaped particles with  $X$ . For the calculation of  $r_{eff}^3$  the values of  $x_r(X)$  and  $x_0$  are taken to be same as that for the linear polarizability case. The sign of the volume has been taken according to the earlier argument. A least squares fit to this plot is also shown in Fig. 8(b). The correlation parameter for this fitting is found to be 0.97. This shows that  $\beta_{xxx}$  de-

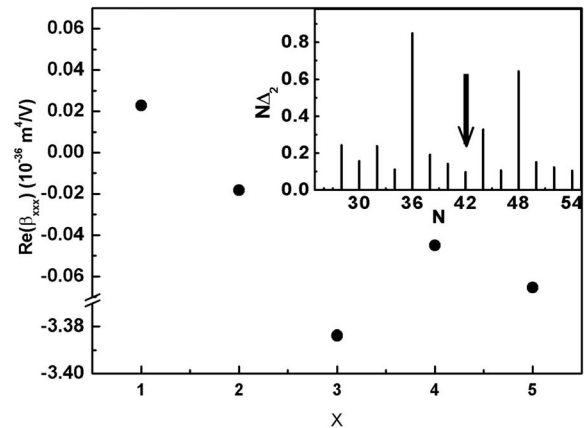


FIG. 10. The static second-order polarizability for sector-shaped nanoparticles containing approximately 40 electrons as a function of  $X$ . Inset shows the plot of  $N\Delta_2$  with  $\Delta_2=E(N+1)+E(N-1)-2E(N)$  for sector with  $X=3$ . The solid arrow denotes the particle having 42 electrons for which the  $\beta_{xxx}$  result is displayed at  $X=3$ .

pends linearly on the product of asymmetric volume and the third power of electron cloud length. Thus, the value of  $\beta_{xxx}$  depends not only on the asymmetric volume but also on the way the volume is distributed. We note here that the trend discussed above is not exhibited by sectors with very small energy difference between the highest occupied and the lowest unoccupied levels ( $E_g$ ). For example, in Fig. 10, we plot the value of  $\beta_{xxx}$  at zero frequency as a function of  $X$  for sectors containing nearly 40 electrons. Note that the magnitude of  $\beta_{xxx}$  for  $X=3$  is rather large compared to the expected trend. For this sector with  $X=3$ , the energy  $E_g$  is 0.007 eV. It is well known that the energy gap  $E_g$  is related to the stability of the particle. Thus, all metal clusters are not equally stable, and the stability of small spherical metal clusters is determined by magic numbers which correspond to shell filling. The stability of a particle of any shape is determined by the quantity  $N\Delta_2$ , where  $\Delta_2=E(N+1)+E(N-1)-2E(N)$ ,<sup>30</sup> where  $E(N)$  denotes total energy of the particle containing  $N$  electrons. In the inset of Fig. 10, we show the plot of  $N\Delta_2$  for sector with  $X=3$ . Note that the sector containing 42 electrons is less stable compared to other sectors of different size. In this paper, we do not consider particles which are less stable.

In Fig. 11, we give the dispersion plots of  $\text{Re}(\beta_{xxx})$  for sectors having  $X=1, 2$ , and 4. To avoid numerical singularities, we add a small complex term  $i0.055$  eV to all frequency denominators in Eq. (8). As expected, the maximum value of  $\beta_{xxx}$  itself shows behavior similar to the static case. The maximum value of  $\beta_{xxx}$  for the case of  $X=2$  is lower than the other cases, while the sign of  $\beta_{xxx}$  at the maximum magnitude of  $\beta_{xxx}$  is negative for all the cases except for the  $X=1$  case. The peak position of  $\text{Re}(\beta_{xxx})$  lies near the resonance of the  $\alpha_{xx}$ , since the expression for  $\beta_{xxx}$  also has a denominator  $(E_{ij}-\omega)$ . Furthermore, there are peaks exactly at half the frequency of resonances of  $\alpha_{xx}$ , which are due to the two-photon resonances. The locations of two-photon resonances can be determined by noting that the expression for  $\beta_{xxx}$  also has a denominator  $(E_{ij}-2\omega)$ , which will lead to a resonance when  $\omega=E_{ij}/2$ . We note here that these two-

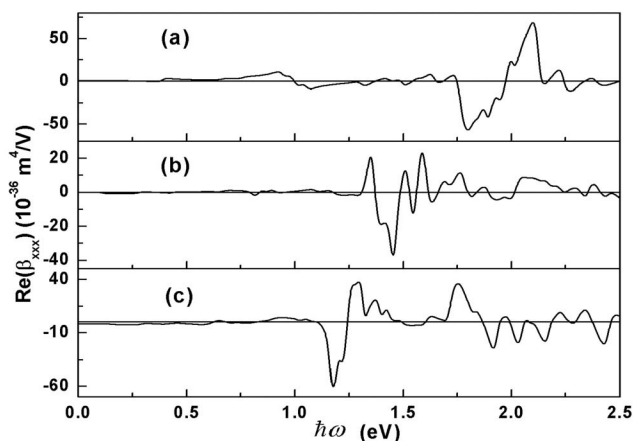


FIG. 11. Real part of  $\beta_{xxx}$  as a function of the photon energy for sector-shaped particles with (a)  $X=1$ , (b)  $X=2$ , and (c)  $X=4$  containing approximately 200 electrons.

photon resonances are important, since the second-harmonic efficiency at these frequencies is high while the linear absorption loss is very low.

#### IV. CONCLUSIONS

In this paper, we reported the effect of shape on the scaling behavior of the linear and second-order nonlinear optical polarizabilities of sector-shaped nanoparticles. In order to calculate the optical response properties, we derived analytical expressions for linear and second-order polarizabilities by using time-dependent perturbation theory. Calculation of polarizabilities using these expressions requires knowledge of wave functions and the corresponding eigenenergies. These were obtained analytically by solving time-independent Schrödinger equation for  $N$  free electrons confined inside a hard walled sector-shaped particle. The wave functions for sector-shaped particles are subset of the wave functions for a spherical nanoparticle of the same radius. Using these wave functions, we calculated the dipole matrix elements and deduced the selection rule for transitions. We found that due to the wave nature of the electrons, the ground state electron density distribution at 0 K is very small near the edges and corners of the nanoparticles. Such low-density regions are found wherever the space available for the electrons is less than half of wavelength of the Fermi electron. This reduction in the length of electron cloud plays an important role in the scaling behavior of linear and second-order polarizabilities.

The static polarizability along any given direction of a sector-shaped nanoparticle is shown to be proportional to the product of number of confined electrons inside the particle and the square of the length of the particle along that direction with a correction for eliminating the low electron density regime. We also defined a quantity called asymmetric volume which is obtained by reflecting the same object onto itself and removing the overlapped volume. We show that this quantity plays an important role in determining the magnitude of second-order polarizability. We found that for par-

ticles with the same volume, the magnitude of  $\beta_{xxx}$  varies linearly as a function of product of asymmetric volume and the cube of effective electron cloud length. The magnitude of  $\beta_{xxx}$  for hemisphere, which is a special case of sector with  $X=1$ , was found to be more than that of a sector with  $\phi_0 = \pi/2$ . This is consistent with larger asymmetric volume of a hemisphere compared to that of a particle with  $\phi_0 = \pi/2$ . The sign of second-order polarizability of hemispherical-shaped particle is different from that of other sectors. This is attributed to a change in the location of tip when compared to the other sectors.

Finally, we note that the connection between the nonlinear optical polarizability and the asymmetric volume established in this paper will be helpful in better understanding of the scaling behavior of nanoparticles, and this will be useful in designing nanoparticles with other shapes which possess large hyperpolarizability.

#### ACKNOWLEDGMENTS

The authors thank S. C. Mehendale for many discussions and critical reading of the paper. J.J. acknowledges helpful discussions with S. M. Oak and Rama Chari.

#### APPENDIX: DERIVATION OF SECOND-ORDER POLARIZABILITY

We consider system of noninteracting  $N$  electrons in a potential  $V_0(\mathbf{r})$  interacting with a time-dependent external electric field  $\mathbf{E}(t)$ ,

$$\mathbf{E}(t) = E_0[e^{i\omega t} + e^{-i\omega t}]\hat{\mathbf{e}}, \quad (\text{A1})$$

where  $\hat{\mathbf{e}}$  is the unit vector in any of the Cartesian coordinates. Using the variational principle, the time-dependent canonical equations for the single-particle orbitals can be written as<sup>24,31</sup>

$$\left[ H^{(0)} + H^{(1)} - i\frac{\partial}{\partial t} \right] \Psi_j(\mathbf{r}, t) = \sum_j \varepsilon_{ij}(t) \Psi_j(\mathbf{r}, t), \quad (\text{A2})$$

where  $H^{(0)}$  and  $H^{(1)}$  are given by

$$H^{(0)} = \left[ -\frac{\nabla^2}{2} + V_0(\mathbf{r}) \right] \quad (\text{A3})$$

and

$$H^{(1)} = -\boldsymbol{\mu} \cdot \mathbf{E}(t), \quad (\text{A4})$$

$\boldsymbol{\mu}$  is the dipole moment operator,  $\varepsilon_{ij}$  are the elements of Lagrangian multiplier matrix, and  $\Psi_i(\mathbf{r}, t)$  are the time-dependent single-particle wave functions. The calculation of  $\beta$  requires knowledge of perturbed orbitals and perturbed  $\varepsilon_{ij}$ . To accomplish this task, we now expand  $\Psi_i$  and  $\varepsilon_{ij}$  in perturbation series with respect to the applied field,

$$\Psi_i = \sum_{m=0}^{\infty} \Psi_i^{(m)}, \quad (\text{A5})$$

$$\varepsilon_{ij} = \sum_{m=0}^{\infty} \varepsilon_{ij}^{(m)}. \quad (\text{A6})$$

Next, we expand  $\Psi_i^{(1)}$  and  $\Psi_i^{(2)}$  in terms of its possible frequency components,

$$\Psi_i^{(1)}(\mathbf{r}, t) = \Psi_i^{(1)}(+1)e^{i\omega t} + \Psi_i^{(1)}(-1)e^{-i\omega t}, \quad (\text{A7})$$

$$\Psi_i^{(2)}(\mathbf{r}, t) = \Psi_i^{(2)}(+2)e^{2i\omega t} + \Psi_i^{(2)}(-2)e^{-2i\omega t} + \Psi_i^{(2)}(0). \quad (\text{A8})$$

In the same way, we can expand the first order of  $H$  and the first and second orders of  $\varepsilon_{ij}$ . The  $(\pm 1)$  in  $\Psi_i^{(1)}(\pm 1)$  represents the amplitude of  $\pm\omega$  Fourier component of  $\Psi_i^{(1)}$  and similarly for the  $(\pm 2\omega)$  case. Using the above equations in Eq. (A2), we get the time-dependent coupled perturbed single-particle equations in different orders and in different frequency components. The zeroth-order equation is

$$H^{(0)}\psi_i^{(0)} = \varepsilon_{ij}^{(0)}\psi_j^{(0)}. \quad (\text{A9})$$

By exploiting the nature of total energy and density under unitary transformation, the  $\varepsilon_{ij}^{(0)}$  matrix can be diagonalized to a form  $\varepsilon_{ij}^{(0)} = \delta_{ij}\varepsilon_i$ .<sup>24</sup> The first-order equations with  $\pm\omega$  frequency components are

$$\begin{aligned} H^{(0)}\Psi_i^{(1)}(\pm 1) \pm \omega\Psi_i^{(1)}(\pm 1) + H^{(1)}(\pm 1)\Psi_i^{(0)} \\ = \sum_j \{ \varepsilon_{ij}^{(0)}\Psi_j^{(1)}(\pm 1) + \varepsilon_{ij}^{(1)}(\pm 1)\Psi_j^{(0)} \}. \end{aligned} \quad (\text{A10})$$

In the same way, the second-order equations with  $\pm 2\omega$  frequency components are given by

$$\begin{aligned} H^{(0)}\Psi_i^{(2)}(\pm 2) \pm 2\omega\Psi_i^{(2)}(\pm 2) + H^{(1)}(\pm 1)\Psi_i^{(1)}(\pm 1) \\ = \sum_j \{ \varepsilon_{ij}^{(0)}\Psi_j^{(2)}(\pm 2) + \varepsilon_{ij}^{(1)}(\pm 1)\Psi_j^{(1)}(\pm 1) + \varepsilon_{ij}^{(2)}(\pm 2)\Psi_j^{(0)} \}. \end{aligned} \quad (\text{A11})$$

Using the normalization condition and parallel transport gauge, we can use the following relations between the various orders of orbitals:<sup>25</sup>

$$\langle \Psi_i^{(0)} | \Psi_j^{(k)} \rangle = \begin{cases} -\frac{1}{2} \sum_{l=1}^{k-1} \langle \Psi_i^{(l)} | \Psi_j^{(k-l)} \rangle & \text{for } k > 1 \\ 0 & \text{for } k = 1. \end{cases} \quad (\text{A12})$$

The second-order polarizabilities can be calculated using

$$\beta_{\sigma\sigma\sigma}(\mp 2\omega) = \int H^\sigma \rho^{\sigma\sigma}(\pm 2) d\mathbf{r}. \quad (\text{A13})$$

For this, we need the various orders of electron density distribution

$$\rho(\mathbf{r}, t) = \sum_i \Psi_i^* \Psi_i. \quad (\text{A14})$$

The second-order frequency components of  $\rho$  is

$$\begin{aligned} \rho^{(2)}(\pm 2) = \sum_i \{ \Psi_i^{*(0)} \Psi_i^{(2)}(\pm 2) + \Psi_i^{*(1)}(\mp 1) \Psi_i^{(1)}(\pm 1) + \Psi_i^{*(2)} \\ \times (\mp 2) \Psi_i^{(0)} \}. \end{aligned} \quad (\text{A15})$$

To derive an expression for  $\beta_{\sigma\sigma\sigma}$ , the following steps are followed.

- (1) Start with the  $+\omega$  part of Eq. (A11) and premultiply with  $\langle \Psi_i^{(1)}(+2) |$ .
- (2) Take the adjoint of  $+\omega$  of Eq. (A10) with  $2\omega$  argument and postmultiply with  $|\Psi_i^{(2)}(+2)\rangle$ .
- (3) Subtract the result of step (2) from the result of step (1).
- (4) Take the adjoint of  $-2\omega$  part of Eq. (A11) and postmultiply with  $|\Psi_i^{(1)}(-2)\rangle$ .
- (5) Premultiply the  $-\omega$  part of Eq. (A10) with  $\langle \Psi_i^{(2)}(-2) |$ .
- (6) Subtract the result of step (4) from the result of step (5).
- (7) Add the result of step (3) and step (6).

Using the resultant equation and the normalization condition, we get

$$\begin{aligned} \langle \Psi_i^{(1)}(+2) | H^{(1)}(+1) | \Psi_i^{(1)}(+1) \rangle - \langle \Psi_i^{(0)} | H^{\dagger(1)}(+2) | \Psi_i^{(2)}(+2) \rangle \\ + \langle \Psi_i^{(1)}(-1) | H^{\dagger(1)}(-1) | \Psi_i^{(1)}(-2) \rangle - \langle \Psi_i^{(2)}(-2) | H^{(1)}(-2) \\ \times | \Psi_i^{(0)} \rangle = \sum_j \{ \langle \Psi_i^{(1)}(+2) | \Psi_j^{(1)}(+1) \rangle \varepsilon_{ij}^{(1)}(+1) - \langle \Psi_j^{(0)} | \Psi_i^{(2)} \\ \times (+2) \rangle \varepsilon_{ij}^{\dagger(1)}(+2) + \langle \Psi_i^{(1)}(-1) | \Psi_j^{(1)}(-2) \rangle \varepsilon_{ij}^{\dagger(1)}(-1) \\ - \langle \Psi_i^{(2)}(-2) | \Psi_j^{(0)} \rangle \varepsilon_{ij}^{(1)}(-2) \}. \end{aligned} \quad (\text{A16})$$

Rearranging and subtracting  $\langle \Psi_i^{(1)}(-1) | H^{(1)}(-2) | \Psi_i^{(1)}(+1) \rangle$  on both sides and summing over  $i$ , we can get

$$\begin{aligned} -\beta_{\sigma\sigma\sigma}(-2\omega) = \sum_{ij} \left\{ \langle \Psi_i^{(1)}(+2) | \Psi_j^{(1)}(+1) \rangle \varepsilon_{ij}^{(1)}(+1) \right. \\ + \langle \Psi_j^{(1)}(-1) | \Psi_i^{(1)}(-2) \rangle \varepsilon_{ij}^{\dagger(1)}(-1) \\ + \frac{1}{2} \langle \Psi_j^{(1)}(-1) | \Psi_i^{(1)}(+1) \rangle \varepsilon_{ij}^{\dagger(1)}(+2) \\ + \frac{1}{2} \langle \Psi_i^{(1)}(-1) | \Psi_j^{(1)}(+1) \rangle \varepsilon_{ij}^{(1)}(-2) \left. \right\} \\ - \sum_i \{ \langle \Psi_i^{(1)}(+2) | H^{(1)}(+1) | \Psi_i^{(1)}(+1) \rangle \\ + \langle \Psi_i^{(1)}(-1) | H^{\dagger(1)}(-1) | \Psi_i^{(1)}(-2) \rangle \\ + \langle \Psi_i^{(1)}(-1) | H^{(-1)}(-2) | \Psi_i^{(1)}(+1) \rangle \}. \end{aligned} \quad (\text{A17})$$

Using  $M_{ai}^\sigma = \langle \Psi_a^{(0)} | \sigma | \Psi_i^{(0)} \rangle$  and the expansion for  $\Psi_i^{(1)}(\pm 1)$ ,

$$|\Psi_i^{(1)}(\pm 1)\rangle = \sum_a \frac{\langle \Psi_a^{(0)} | \sigma | \Psi_i^{(0)} \rangle}{\varepsilon_a^0 - \varepsilon_i^0 \mp \omega} |\Psi_a^{(0)}\rangle, \quad (\text{A18})$$

we can write

$$\beta_{\sigma\sigma\sigma}(-2\omega; \omega, \omega) = \frac{-1}{2\hbar^2\epsilon_0} \left\{ \sum_{iab} \left[ \frac{M_{ab}^\sigma M_{ia}^\sigma M_{bi}^\sigma}{(\omega_{ia} + 2\omega)(\omega_{bi} - \omega)} + \frac{M_{ab}^\sigma M_{ia}^\sigma M_{bi}^\sigma}{(\omega_{ia} - \omega)(\omega_{bi} + 2\omega)} + \frac{M_{ab}^\sigma M_{ia}^\sigma M_{bi}^\sigma}{(\omega_{ia} - \omega)(\omega_{bi} - \omega)} \right] - \sum_{ija} \left[ \frac{M_{ij}^\sigma M_{ia}^\sigma M_{aj}^\sigma}{(\omega_{ia} + 2\omega)(\omega_{aj} - \omega)} + \frac{M_{ij}^\sigma M_{ia}^\sigma M_{aj}^\sigma}{(\omega_{ja} - \omega)(\omega_{ai} + 2\omega)} + \frac{M_{ij}^\sigma M_{ia}^\sigma M_{aj}^\sigma}{2(\omega_{ja} - \omega)(\omega_{ai} - \omega)} + \frac{M_{ij}^\sigma M_{ia}^\sigma M_{aj}^\sigma}{2(\omega_{ia} - \omega)(\omega_{aj} - \omega)} \right] \right\}. \quad (\text{A19})$$

- 
- <sup>1</sup>J. J. Monk, M. Barbic, D. R. Smith, D. A. Schultz, and S. Schultz, *J. Chem. Phys.* **116**, 6755 (2002).
- <sup>2</sup>K. Lance Kelly, Eduardo Coronado, Lin Lin Zhao, and George C. Schatz, *J. Phys. Chem. B* **107**, 668 (2003).
- <sup>3</sup>Olivier J. F. Martin, *Optical Nanotechnologies: The Manipulation of Surface and Local Plasmons*, edited by J. Tominaga and D. P. Tsai (Springer, Heidelberg, 2002), Chap. 13, pp. 203–228, and references therein.
- <sup>4</sup>B. Lamprecht, A. Leitner, and E. R. Aussenegg, *Appl. Phys. B: Lasers Opt.* **68**, 419 (1999).
- <sup>5</sup>B. Lamprecht, J. R. Krenn, A. Leitner, and F. R. Aussenegg, *Phys. Rev. Lett.* **83**, 4421 (1999).
- <sup>6</sup>Christy L. Haynes, Adam D. McFarland, LinLin Zhao, Richard P. Van Duyne, George C. Schatz, Linda Gunnarsson, Juris Prikulis, Bengt Kasemo, and Mikael Kall, *J. Phys. Chem. B* **107**, 7337 (2003).
- <sup>7</sup>L. Genzel, T. P. Martin, and U. Kreibig, *Z. Phys. B* **21**, 339 (1975).
- <sup>8</sup>W. A. Kraus and G. C. Schatz, *J. Chem. Phys.* **79**, 6130 (1983).
- <sup>9</sup>F. Hache, *J. Opt. Soc. Am. B* **3**, 1647 (1986).
- <sup>10</sup>M. Barma and V. Subrahmanyam, *J. Phys.: Condens. Matter* **1**, 7681 (1989).
- <sup>11</sup>R. Jin, *Science* **294**, 1901 (2001).
- <sup>12</sup>Mathieu Maillard, Pinray Huang, and Louis Brus, *Nano Lett.* **3**, 1611 (2003).
- <sup>13</sup>K. K. Caswell, Christopher M. Bender, and Catherine J. Murphy, *Nano Lett.* **3**, 667 (2003).
- <sup>14</sup>Jinxin Gao, Christopher M. Bender, and Catherine J. Murphy, *Langmuir* **19**, 9065 (2003).
- <sup>15</sup>Yugang Sun and Younan Xia, *Science* **298**, 2176 (2002).
- <sup>16</sup>J. P. Kottmann, O. J. F. Martin, D. R. Smith, and S. Schultz, *J. Microsc.* **202**, 60 (2001).
- <sup>17</sup>J. Jayabalan, M. P. Singh, and K. C. Rustagi, *Phys. Rev. B* **68**, 075319 (2003).
- <sup>18</sup>Hemmo Tuovinen, Martti Kauranen, Konstantins Jefimovs, Pasi Vahimaa, Thomas Vallius, Jari Turunen, Nikolai V. Tkachenko, and Helge Lemmetyinen, *J. Nonlinear Opt. Phys. Mater.* **11**, 421 (2002).
- <sup>19</sup>Amanda J. Haes, Shengli Zou, George C. Schatz, and Richard P. Van Duyne, *J. Phys. Chem. B* **108**, 6961 (2004).
- <sup>20</sup>Molly M. Miller and Anne A. Lazarides, *J. Phys. Chem. B* **109**, 21556 (2005).
- <sup>21</sup>Andrew M. Moran, Jiha Sung, Erin M. Hicks, Richard P. Van Duyne, and Kenneth G. Spears, *J. Phys. Chem. B* **109**, 4501 (2005).
- <sup>22</sup>K. Li, M. I. Stockman, and D. J. Bergman, *Phys. Rev. B* **72**, 153401 (2005).
- <sup>23</sup>N. I. Zheludev and V. I. Emel'yanov, *J. Opt. A, Pure Appl. Opt.* **6**, 26 (2004).
- <sup>24</sup>S. P. Karna and M. Dupuis, *J. Comput. Chem.* **12**, 487 (2004).
- <sup>25</sup>X. Gonze, *Phys. Rev. A* **52**, 1096 (1995).
- <sup>26</sup>H. Gohlich, T. Lange, T. Bergmann, and T. P. Martin, *Phys. Rev. Lett.* **65**, 748 (1990).
- <sup>27</sup>Charles Kittel, *Introduction to Solid State Physics*, 7th ed. (Wiley, New York, 2004).
- <sup>28</sup>Jorg P. Kottmann, Olivier J. F. Martin, David R. Smith, and Sheldon Schultz, *Phys. Rev. B* **64**, 235402 (2001).
- <sup>29</sup>Jorg P. Kottmann and Olivier J. F. Martin, *Appl. Phys. B: Lasers Opt.* **73**, 299304 (2001).
- <sup>30</sup>J. A. Alonso and L. C. Balbas, *Top. Curr. Chem.* **182**, 119 (1996).
- <sup>31</sup>Arup Banerjee, Jochen Autschbach, and Tom Ziegler, *Int. J. Quantum Chem.* **101**, 572 (2005).